Exp Fluids (2010) 48:983–997
DOI 10.1007/s00348-009-0777-4

RESEARCH ARTICLE

Three-dimensional, three-component wall-PIV

André Berthe · Daniel Kondermann · Carolyn Christensen · Leonid Goubergrits · Christoph Garbe · Klaus Affeld · Ulrich Kertzscher

Received: 16 November 2007 / Revised: 12 October 2009 / Accepted: 16 October 2009 / Published online: 18 November 2009

Abstract This paper describes a new time-resolved three-dimensional, three-component (3D-3C) measurement technique called wall-PIV. It was developed to assess near wall flow fields and shear rates near non-planar surfaces. The method is based on light absorption according to Beer–Lambert's law. The fluid containing a molecular dye and seeded with buoyant particles is illuminated by a monochromatic, diffuse light. Due to the dye, the depth of view is limited to the near wall layer. The three-dimensional particle positions can be reconstructed by the intensities of the particle's projection on an image sensor. The flow estimation is performed by a new algorithm, based on learned particle trajectories. Possible sources of measurement errors related to the wall-PIV technique are analyzed. The accuracy analysis was based on single particle experiments and a three-dimensional artificial data set simulating a rotating sphere.

1 Introduction

The instantaneous measurements of near wall flows are of great interest in biomedical research in order to obtain a deeper understanding of physiological and pathological processes. In biofluid mechanics, some of the most interesting parameters linking biological processes with hemodynamics are wall shear rate and wall shear stress. Many medical issues, such as thrombotic events and atherosclerosis, can be attributed to these specific parameters near non-planar, deformable walls (Affeld et al. 2004; Goubergrits et al. 2002). Examples of where these medical issues occur are aneurysms and displacement blood pumps (Berthe et al. 2008; Kertzscher et al. 2008. To obtain wall shear rate and wall shear stress, a 3D-2C measurement technique would be sufficient. However, the third velocity component (normal to the wall) is also of great interest, for example, for the modelling of thrombus formation (Kim et al. 2006). The measurement of flow fields and shear rates near non-planar walls is challenging for existing three-dimensional, three-component (3D-3C) measurement techniques, such as 3D-PTV, holographic PIV, defocusing PIV and tomographic PIV (Fomin 1998). The applicability of these techniques is discussed in the following section.

In contrast to the existing 3D-3C measurement techniques, the wall-PIV technique was specially developed to overcome the problems related to flow measurements near vaulted and/or deformable walls (Kertzscher et al. 1999). Important is the difference between a vaulted and a curved wall: A vaulted wall is a wall with two non-vanishing principle curvatures, a curved wall has only one non-vanishing principle curvature.

The wall-PIV technique uses tracer particles for the visualization and measurement of flows in an illuminated fluid layer adjacent to a possibly vaulted and deformable wall. This layer is generated by a monochromatic full-field illumination of the flow model, whereas the depth of view is limited by a molecular dye added to the test fluid and by the light intensity. This is a modification of the classical

A. Berthe (✉) · C. Christensen · L. Goubergrits · K. Affeld · U. Kertzscher
Biofluid Mechanics Laboratory, Charité - Universitätsmedizin Berlin, Thielallee 73, 14195 Berlin, Germany
e-mail: andre.berthe@charite.de

D. Kondermann · C. Garbe
Digital Image Processing Research Group, Heidelberg Collaboratory for Image Processing, University of Heidelberg, Speyerer Straße 4, 69115 Heidelberg, Germany
e-mail: daniel.kondermann@iwr.uni-heidelberg.de

PIV method, which uses a planar laser light sheet for illumination. The dye leads to an attenuation of the intensity of the brightness of the particle's projection directly related to the particle's distance to the wall. Measuring the brightness of the particle's projection in addition to its displacement makes a full 3D measurement possible. In contrast to other 3D PIV techniques (see sect. 2), only a single camera is required for image acquisition. This represents a major advantage in measurement tasks with limited access. Consequently, an assessment of shear rates and shear stresses becomes viable in these situations. In wall-PIV, the particle grey intensities are not treated as invariants, as in classical PIV, but are explicitly accounted for in the flow-measuring algorithm to make feasible the extraction of three-component field measurements (Jehle et al. 2006). The accuracy analysis is based on single particle experiments, of which one was used as a calibration procedure. To identify errors caused by the flow estimation algorithm, numerical tests with artificial data sets were performed.

2 Related 3D-3C techniques

The main motivation for the development of wall-PIV is the need for a time-resolved measurement technique which is optimized for the evaluation of near wall flow fields and wall shear stresses near vaulted, possibly deforming walls. These parameters can be obtained from knowledge of the fluid flow velocity at a known distance from the wall.

Many methods for 3D-3C flow field estimation have been proposed. One can distinguish between point-measurement, line-measurement, and field-measurement techniques. Point- and line-measurement techniques are, for example, Preston tubes, surface hot films, hot wires, surface fences, or laser doppler velocimetry (also including variations, such as the ultrasonic doppler method (Takeda 1999) or the laser Doppler profile sensor (Modarress et al. 2005). Even though they were optimized for the measurement of near wall flow fields, they cannot instantaneously and simultaneously estimate the flow within the whole region of interest (ROI). Furthermore, such approaches require extensive and time-consuming measurement series. A possible solution for this problem would be the application of whole arrays of micro-electromechanical system (MEMS) sensors (Sheplak et al. 2004). However, the application of such arrays on complex vaulted surfaces for field measurements is challenging. Especially for flexible surfaces, this can be an impossible task.

In addition to point- and line-measurement methods, several field-measurement techniques are able to measure 3D near wall flow fields. Examples are laser photochromic velocimetry (Park et al. 1999) and particle image velocimetry (PIV) (Westerweel 1993). For 3D-3C PIV, many methods have been developed, including scanning PIV (Bruecker 1995; Triep et al. 2005), defocusing PIV (Graff et al. 2008), holographic PIV (Kim and Lee 2008), tomographic PIV (Elsinga et al. 2006), laser light sheet tomography (Bruecker 1995), and 3D-PTV (Maas et al. 1993; Malik et al. 1993). The advantages and disadvantages of most of these techniques are well reviewed in (Elsinga et al. 2006; Kertzscher et al. 2008). Only a few of them can be used at vaulted walls and will be discussed here. Therefore, we will first consider three of the principle differences between wall-PIV and current 3D-3C methods.

- The current 3D-3C methods are optimized (resolution and accuracy) for a measurement volume that is fixed in space, normally hexahedral in shape and cannot be restricted to the non-planar, near wall region. These methods are less accurate for measurements near the wall, since they were not primarily designed to measure near-wall conditions where high-velocity gradients, low velocities in comparison to the mean velocities, and optical distortions may appear.
- All particle based methods are capable of recording a certain maximum particle density within the measurement volume. If a thin layer adjacent to the vaulted wall and therefore only a minor part, or region, of the entire measurement volume is of interest (ROI), then the maximum number of vectors within the ROI is noticeably less than within the total volume. This results in a greatly reduced resolution of the near-wall measurement.
- The determination of the exact distance between a flow vector and the wall represents a challenge to all of these techniques as the exact position of the wall also has to be determined.

Furthermore, each of the earlier mentioned techniques has specific disadvantages for the selected field of investigation, which motivated us to develop the wall-PIV technique.

The scanning PIV approach (Bruecker 1995) is still limited in its temporal resolution as the light sheet of a 2C or 3C (stereo) PIV setup is displaced normal to its plane. The flow structure can be reconstructed as long as the scanning time of the investigated volume is small compared to the characteristic time scale of the flow. For the investigation of thin (several hundreds of micrometres) near wall regions, the experimental setup of a scanning PIV system is complicated. Reflections and the alignment of the laser sheet limit the applicability of this and similar systems, such as (Kaehler and Kompenhans 2000; Ruck 2003).

Holographic PIV seems to provide a high potential for the assessment of near wall flows. For vaulted walls, one problem would be the necessary depth resolution which is limited in holographic PIV (see (Hinsch 2002) for details). Until now, most measurements are based on holographic films instead of CCD cameras, resulting in high processing times. This is caused by the relatively low number of vectors that can be obtained with current CCD sensors (Hill et al. 2008). However, this limitation of holographic PIV can be resolved with the development of new high-resolution CCD sensors.

The identification of particles in images acquired by cameras with different spatial orientations is used by defocusing digital PIV (DDPIV) and 3D-PTV. For both techniques, the possible particle density and therefore the number of assessed velocity vectors is limited, whereas Hill et al. (2008) state that the seeding density of DDPIV can be higher than in PTV. The spatial resolution of DDPIV, also known as volumetric three-component velocimetry, can be up to 10 µm for the planar resolution and 40 µm for the depth resolution. Image processing times are relatively low with 1 to 5 min per volume. A complication of this approach is the appearance of so-called "ghost-particles", ambiguities of the particles' positions resulting from the reconstruction approach (Lai et al. 2008). The DDPIV approach requires a plane flow model surface, aligned perpendicularly to the camera-setups' centreline, which is unfavourable for vaulted walls.

Tomographic PIV uses the same camera setup as 3D-PTV, utilizing an expanded laser sheet and typically four instead of three cameras. According to Elsinga et al. (2006), the technique can handle approximately 10 times higher particle densities than 3D-PTV. With an optimal particle density of at least 15 particles per interrogation window for PIV, according to Keane and Adrian (1990), the resulting density of the vector fields is comparable to that of 3D-PTV. As in DDPIV, ghost particles can affect the result. According to Michaelis and Wieneke (2008), the number of ghost particles depends strongly on the number of cameras and the particle diameter. As a result, a higher quality can be obtained by a higher complexity of the measurement setup. Compared to DDPIV and wall-PIV, this technique has a high processing time of about 30 min to 1 h per volume (Schroeder et al. 2008; Atkinson et al. 2008).

Some medical measurement techniques, such as magnetic resonance imaging (MRI) and echocardiography, also allow the three-dimensional measurement of flow fields. However, their spatial and temporal resolutions are not yet sufficient for the investigation of near wall flow fields (Köhler et al. 2001; Xie et al. 2005).

3 Wall-PIV

3.1 From Beer–Lambert to wall-PIV

The wall-PIV technique uses a monochromatic full-field illumination with the light sources placed next to a high-speed camera (CCD or CMOS) to acquire the movement of tracers seeded in a dyed fluid in a transparent flow model. The emitted light is absorbed by the dyed fluid, so that only tracers in a thin ROI are visible. As long as this layer is within the depth of focus of the camera, the shape or eventual movements of the wall will have no major impact on the measurements. In addition, the refractive index is matched in order to minimize aberrations caused by vaulted walls. Thus, the principal innovation of the wall-PIV technique is the application of light absorption according to Beer–Lambert's law:

$$I = I_0 \cdot e^{-\varepsilon \cdot c \cdot R} \tag{1}$$

This law quantifies the intensity extinction I of an emitted light I_0 by passing a distance R through an absorbing fluid with the absorbance coefficient ε and the concentration c of the absorbing substance. By using a molecular dye, problems related to inhomogeneities of absorption and scattering are avoided. Since ε of the dyed fluid and the given monochromatic light is known, the penetration depth, and therefore the thickness of the layer, can be controlled. As illustrated in Fig. 1, particles traversing the illuminated region reflect the light, which is acquired by a camera mounted next to the light source. Particles near the wall appear brighter than particles farther away from the wall. This, together with the x- and y-position of the particle in the image, allows the particle's three-dimensional position to be

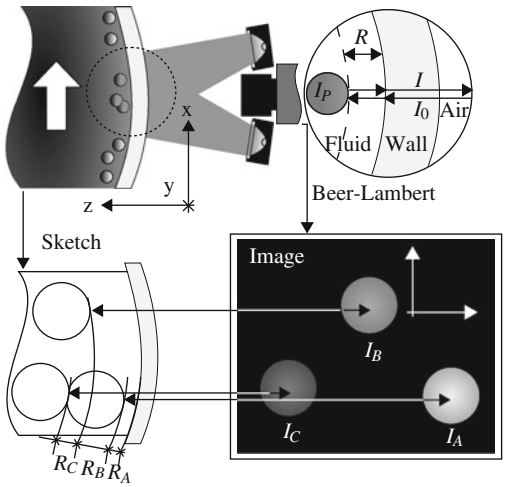

Fig. 1 Principle of the measurement technique: Reduction of light intensity due to absorption. *Particle A* is closer to the wall than *particle B* ($R_A < R_B$) and appears brighter in the image ($I_A > I_B$)

obtained. The reflection of a particle is recorded by the camera chip as a grey value, which corresponds to a given distance between the particle's surface and the wall. Note that a single particle scattering model may be assumed because of the relatively large distance between particles. Classical PIV experiments recommend about 15 particles per 32 × 32 pixel interrogation area (Keane and Adrian 1990). Our experiments found significantly lower particle concentrations in a near wall region, i.e., an average of 0.4 particles per 32 × 32 pixel area during investigations of cerebral vessels (Goubergrits et al. 2009). Having particle reflections with a diameter between 3 and 8 pixels, we can conclude that optical interference between the neighbouring particles can be neglected.

Since the particle moves with its centre of mass, the corresponding velocity vector results from the calculated depth plus the particle radius, which has to be known. As a result, tracer particles have to be monodisperse and spherical.

Since $\varepsilon_{\text{fluid}} \gg \varepsilon_{\text{air}}$, only the distance between the surface and the particle has a relevant influence on the brightness (see Sect. 6). The light intensity I_0 decreases exponentially on the path through the fluid to the particle. Assuming total reflection with the intensity I_p on the particle, the light is absorbed again on its way back and reaches its emission value I on the inner surface of the wall. With the given absorbance coefficient ε and the dye concentration c, we obtain:

$$I = I_p \cdot e^{-\varepsilon \cdot c \cdot R} = I_0 \cdot e^{-2 \cdot \varepsilon \cdot c \cdot R} \tag{2}$$

Thereby, the distance between the particle's surface and the wall can theoretically be calculated for a monochromatic light. However, in reality, there are several deviations from this general theory: The absorbance of the investigated model is, for instance, non-zero, the light is not exactly monochromatic nor has a constant intensity and the particles neither provide a total reflectance nor have exactly the same diameter. To compensate for some of these errors, a calibration and/or modification of the setup can be applied. Both are further described in Sect. 4.1. A detailed error analysis is presented in Sect. 6.

3.2 Major components of our measurement setup

Two different cameras were used in different experiments. The first was a Fastcam Super10K (Photron, Tokyo, Japan) with a resolution of 512 × 480 pixels (px). This CCD camera has a maximum frame rate of 250 full frames per second (fps) and can cache a series of 546 frames. The second camera used was a Redlake MotionPro X-3 (Imaging Solutions GmbH, Eningen, Deutschland). This CMOS camera has a resolution of 1,280 × 1,025 px and a maximum frame rate of 2,000 fps. A total of 6,548 frames can be acquired in a single measurement. We used a Nikkor 50 mm 1:1.8 (Nikon, Tokyo, Japan) lens either in normal or in inverse mounting.

As a molecular dye, we used patent blue V (Schumann and Sohn, Karlsruhe, Germany) with a concentration of $0.3\frac{g}{l}$.

The particles we used were silver-coated hollow ceramic spheres (Potters Industries Inc., Carlstadt, USA) that were sieved to a particle size distribution of 73 to 75 µm.

For illumination, we used 3 W Luxeon light-emitting diodes (LEDs) with wavelengths of $\lambda_1 = 617$ nm and $\lambda_2 = 627$ nm. Plots of the two LED spectra and of the wavelength-dependent transmission of patent blue V are plotted in Fig. 2. For the inclined single particle traversal (see Sect. 4.2), we used a ring light of eight LEDs (four with $\lambda_1 = 617$ nm and four with $\lambda_2 = 627$ nm). The calibration experiment in Sect. 4.1 was realized with two light panels, each of them assembling 104 LEDs; 48 with a wavelength of $\lambda_1 = 617$ nm and 56 with a wavelength of $\lambda_2 = 627$ nm. The illumination can be switched between the two wavelengths by a trigger pulse. The intensity of each wavelength can be defined digitally. For all experiments presented in this manuscript, only the red LEDs of the light panel were used (see Sect. 6 for the potential use of the red-orange LEDs). For more details on the light source see (Schneider et al. 2008).

3.3 Flow estimation

We have developed and tested several flow estimation algorithms for wall-PIV. Many well-elaborated, global

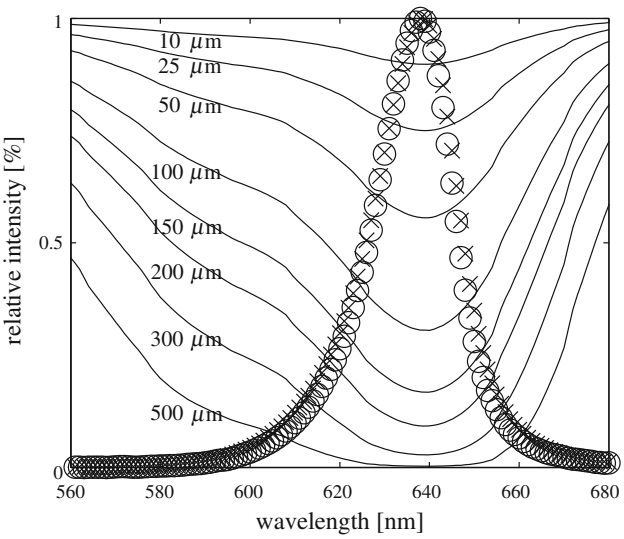

Fig. 2 Transmission of patent blue V and relative spectra of the used LEDs. The wavelength-dependent transmission is *plotted* for different path lengths, for the spectra the relative intensities ι are plotted over the wavelength. *Crosses* represent the red wavelength, *circles* the red-orange wavelength

optical flow (OF) algorithms used for PIV, e.g. (Ruhnau and Schnörr 2007), regularize the two-dimensional flow field while ignoring the actual three-dimensionality of the projected motion and are therefore disadvantageous for applications on volumes with large velocity gradients in the depth (direction normal to the wall). The initial approach for the full 3D-3C flow estimation was to split up the ROI into a set of wall-parallel layers according to the grey values of the recorded particles (Debaene et al. 2005). Afterwards, a cross-correlation was applied on every layer to obtain multiple wall-parallel 2D-2C vector fields. However, as noted in Sect. 3, the image data contains enough information to calculate the whole 3D-3C flow field. Using the grey value of every particle to calculate its distance to the wall, we can obtain a reconstruction of three-dimensional particle positions. Since the depth of our ROIs is very small (approximately 300 μm), this has an influence on the two following factors: the used particle densities in the near wall region are generally relatively low and the velocity gradient orthogonal to the wall is large. As a result, we decided against the 3D cross-correlation procedure (see e.g., (Elsinga et al. 2006)). A second approach utilizes OF algorithms in conjunction with PTV (Jehle and Jähne 2008). In this technique, the particle centres are first segmented using a region growing algorithm, then the three velocity components are computed with a 3D-3C OF algorithm and the particle trajectories are extracted by PTV. This PTV algorithm utilizes the calculated velocity of a given particle to find the best matching for x, y and z coordinates in the subsequent image. The reliability of this method was validated with a falling film by Jehle and Jähne (2008). However, a few disadvantages of the OF algorithm applied by Jehle exist: For example, the algorithm relies on the exact estimation of image derivatives, which is difficult with particle projections of just a few pixels in size. Furthermore, it assumes flow vector magnitudes smaller than one pixel. This motivated us to improve further the flow estimation algorithm.

3.4 Flow estimation algorithm

The new flow estimation algorithm is described in (Kondermann et al. 2008) and aims at maximizing the use of temporal information and minimizing spatial regularization by learning a parametric model of motion describing all plausible or typical trajectories which might occur in a given application. By means of a similarity measure indicating the ability of a given set of model parameters to describe the motion in the sequence, particle velocities can be estimated by optimizing the parameters for maximum similarity values. Thus, similar to the approach of Jehle et al. (2008), on the one hand, trajectory information is used similar to PTV algorithms, but on the other hand, image information is used similar to PIV algorithms. This enables us to combine the advantages of both methods in a hybrid approach (see e.g. (Keane et al. 1995; Cowen et al. 1997) for other hybrid approaches).

Apart from the high accuracy, the main advantage of our approach is that the type of prior knowledge incorporated into the flow estimation process is learned and not defined by an algorithm design. If a good motion model is already known, or a generic model is sufficient, it can also be directly used with our approach.

To give a better understanding of how temporal information is exploited, we formalized the trajectory model as follows: let a given image sequence I be defined on a time interval $[0, T]$ as

$$I : \Omega \times [0, T] \rightarrow \mathbb{R}, \Omega \subset \mathbb{R}3 \tag{3}$$

where $I(\mathbf{x}, t)$ denotes an intensity value of the image sequence at location $\mathbf{x}$ in frame t (i.e. at time t). In our case, the trajectory model consists of the mean vector of all training samples $\mathbf{m}$ together with vectors spanning a linear subspace, which are combined in the columns of a matrix M. Let n be the number of model parameters (i.e. basis vectors of the linear subspace) and L the length of the trajectories in time. A trajectory can then be computed using a parameter vector $\mathbf{p} \in \mathbb{R}^{n\times 1}$ so that:

$$\mathbf{u}(\mathbf{p}) = M\mathbf{p} + \mathbf{m}, \mathbf{m} \in \mathbb{R}^{2L\times 1}, M \in \mathbb{R}^{2L\times n} \tag{4}$$

The resulting vector $\mathbf{u}(\mathbf{p})$ contains trajectory flow vectors for each time step in lexicographic order.

The trajectory model can be acquired by means of unsupervised learning techniques. We chose a standard proper orthogonal decomposition (POD). The concept of POD is to find a lower dimensional basis system with decorrelated axes, which preserves most of the variance in the sample data set and can be used to approximate the trajectories with only a few parameters. Such a basis system consists of the eigenvectors corresponding to the largest eigenvalues of the covariance matrix of the samples.

Once we have learned the model, we can fit it to the image data. Details on the fitting of the trajectory to the image sequence by means of non-linear optimization are laid out in (Kondermann et al. 2008). Here, we give a short summary on this topic.

As is common for PTV algorithms, we first find particle locations. However, these locations are not used to analyze the correspondences as is done in PTV. Instead, we use this information to reduce the computation time of subsequent steps. Once a particle location is found, we create an actual trajectory from a set of initial model parameters using Eq. (4). This initial guess can be computed by any fast motion estimation technique which either yields a trajectory (as e.g. any PTV method) or a dense motion field from

which trajectories can be extracted by interpolation techniques (such as the optical flow method of Horn and Schunck (1981). We then align the trajectory with the image sequence, centreing it around the particle location we found before. Therefore, the trajectory pierces the frames of the sequence at unique locations. To compute the quality of the fit, we compare the intensities at these locations. Ideally, the intensities along the trajectory should correspond to Beer–Lambert's law. To simplify these assumptions, we discovered through experiments that a brightness constancy assumption suffices. Therefore, we minimize the squared intensity differences along the trajectory and yield the results presented here. This energy formulation is non-linear and non-convex but the parameter space is small due to the learned model. Please refer to (Kondermann et al. 2008) for more details on the used energy formulation and optimization schemes.

4 Single particle setup

The basic idea of a single particle setup (SPS) is based on the ability to move one particle precisely in three dimensions. In the following, we present the use of SPS for a wall-PIV calibration and for an investigation of the flow estimation accuracy.

4.1 Calibration

Our wall-PIV SPS system calibration is based on well-defined particle traversals under realistic measurement conditions. This means, all of the measurement components are set up as in a normal measurement but without buoyant tracer particles in the fluid. Instead, a single particle is attached to a traverse and can be precisely positioned. For a calibration experiment, the flow model is replaced by a simple measurement cell to facilitate the monitoring of the vertically traversed particle. By correlating the measured grey values to the corresponding particle depths, the exponential decay of the reflected light can be determined. The reference intensity I_0 and the corresponding grey value ϕ_0 are given to a particle adjacent to the inner surface of the wall. The calibration setup is shown in Fig. 3.

The particle *P* was observed from the bottom and the front of the setup. The bottom view simulates the visible aspect of a wall-PIV setup, whereas the front view allows the distances of the particle to the bottom wall to be measured. The 73-μm diameter particle is glued to a glass cannula with an outer diameter of 30 μm (see Fig. 4).

The cannula was mounted to a micrometre traverse *T*, allowing the particle to be raised and lowered as desired. A separate micrometre measuring dial MD was attached to the micrometre screw in order to provide positioning with up to 5 μm accuracy. The CMOS camera C1 was focused on the measurement cell from the bottom using a Nikon Nikkor 50 mm 1:1.8 lens, a 31 mm and an 18 mm distance ring. A Samsung NV7 OPS digital camera (C2) was

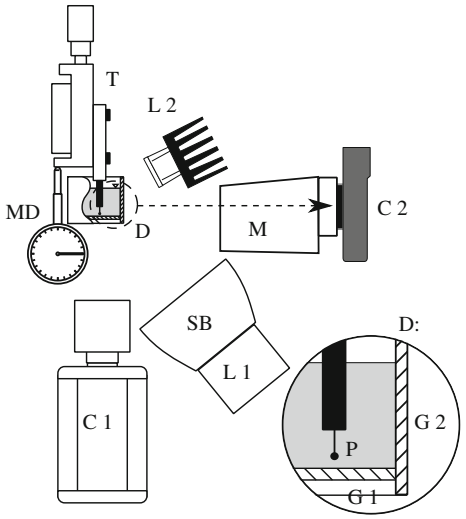

Fig. 3 System setup: Mounted on a traverse T, positioned according to the measurement dial MD, the particle P is immersed into the reservoir, which is filled with dyed fluid (see detail *D*). From the bottom of the wall-PIV setup, a camera C1, using as a light source a light cube L1 with mounted softbox SB, records the particle through a window G1. The particle's distance to the window G1 is recorded from the front through the window G2 by a camera C2, which is mounted on a microscope M. For these records, the white light source L2 is activated

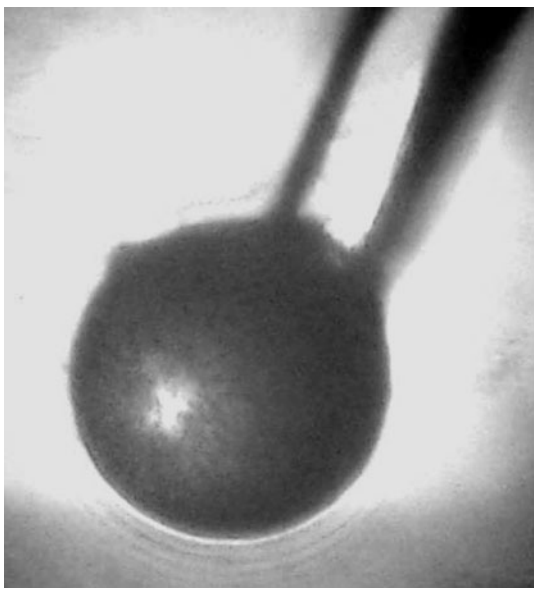

Fig. 4 Particle used during calibration. The glass cannula is located in the *top right corner*. During the calibration, it was on *top* and therefore invisible

attached to the microscope M and was focused on the measurement cell from the front. Mounted parallel to the microscope lens, a white Luxeon Lumiled 5 Watt LED L2 was used as a light source for the front view. During the experiment, the measurement cell was filled with distilled water mixed with patent blue V at a ratio of 0.3 g patent blue V / 1 l dist. H_2O. The experiment involved lowering the particle in 10 µm increments and recording each position with the Samsung camera using only the white LED L2 as a light source. Using the CMOS camera, images were captured with 627 nm (red) and 617 nm (red-orange) light (light panel L1). During these measurements, the white illumination (L2) was deactivated. The grey value corresponding to I_0 was acquired by camera C1, while the vertical positioning of the particle in relation to the bottom glass G1 was recorded by microscopic photos from the camera C2. From each data set acquired by camera C1, the brightest pixel of the particle in an image sequence was located and averaged over the entire sequence. This resulted in a grey value for the particle which was then assigned to the measured distance to the wall. Having recorded the value of the measurement dial MD at the moment of particle-wall contact, we also know all of the particle positions during its traversal with the accuracy of the measurement dial. Furthermore, knowing the grey value corresponding to the intensity I_0 of the particle, we can calculate its positions during traversal with Eq. (11). Note that the two spectra and the wavelength-dependent transmission of patent blue V are known (see Fig. 2).

The results from the calibration and also of the other experiments are in the results section.

4.2 Inclined single particle traversal

The results of the calibration procedure presented in Sect. 4.1 show that the third dimension (the distance between particle and wall) can be obtained with an accuracy of less than 2 µm or 2.3% of the particle diameter. However, for an accuracy analysis of the measurement technique, the presented flow estimation algorithm should be tested. The measurement accuracy of the third dimension and third velocity component should also be compared to that of the first and second components. For this purpose, single particles are moved to defined measurement points, where they are recorded by the original wall-PIV setup. To ensure the exact 3D-movement of a particle, a high precision, three-dimensional traverse system is required. Using the camera Fastcam Super10K and an inversely mounted Nikon Nikkor 50 mm 1:1.8 lens, our setup had a fixed focal distance of 143 mm and a resolution of 68 px/mm. Aiming for a targeted accuracy of up to 1/100 px for the reference data, a precise movement of less than a micrometre had to be assured. This precision is reached by a high-precision milling cutter (at the Department of Precision Engineering and Micro Technology (MFG), TU Berlin), which allows a movement accuracy up to 100 nm in all three directions. Our optical setup was placed on this milling cutter so that single particle measurements with a three-dimensional movement of the particle close to the transparent surface could be realized. A particle P is mounted at the head of the milling cutter t where it can be traversed in all three dimensions. The setup is similar to that in Fig. 3, using the milling cutter as 3D traverse and a chromatic sensor (Fries Research and Technology–FRT GmbH, Germany) with an accuracy of 20 nm, measuring the particle's distance to the glass surface. For further details of the setup see (Berthe et al. 2007).

Using this system, particles with a diameter between 50 µm and 120 µm were investigated. They were moved on ten different reference curves in order to test the measurement technique. Three of these curves are shown in Fig. 5.

The further discussion focuses on the sequence of a descending particle shown on the right of Fig. 5. The particle with a 70 µm diameter was moved in 100 even steps in the horizontal direction by a total of a 1,000 µm and 150 µm in the vertical direction. The last vertical position of the particle corresponds to the particle touching

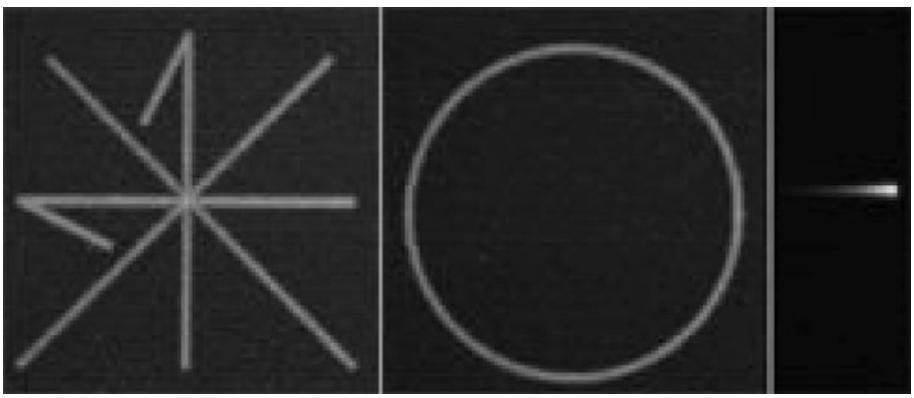

Fig. 5 From *left to right*: complex planar and circular particle path traces, a descending particle trace

the inner surface of the wall. As a result, the centre of the particle was moved from 185 to 35 μm depth.

5 Artificial data sets

In order to further evaluate the accuracy of our flow estimation algorithm, we applied it to synthetically generated data. Unfortunately, no standard data exists up to now that incorporates the application of Beer–Lambert's law to the intensity of particle images for the estimation of 3D-3C flows. We created a new test sequence (available upon e-mail request) of a three-dimensional sphere rotating in space, as illustrated in Fig. 6.

To simulate the image acquisition process, we carried out the following procedure: The radius of the sphere was adjusted so that its minimum and maximum depths yield the brightest, respectively darkest, particle image possible according to Beer–Lambert's law. The maximum particle intensity was computed with Eq. (2). According to Adrian and Yao (1985) and Marxen et al. (2000), the particle shape can be approximated by a 2D-Gaussian function, which we sampled with a variance σ of 2 px for each particle location. We cropped the sampling process at 3σ, where it reached the precision of our 8-bit camera. Two hundred particles were randomly and uniformly distributed within the sphere. The radius of the sphere was set to 150 px. Some particles overlapped partially or totally, so that around 120 particle images could be recognized by the particle detection routine, depending on the noise level.

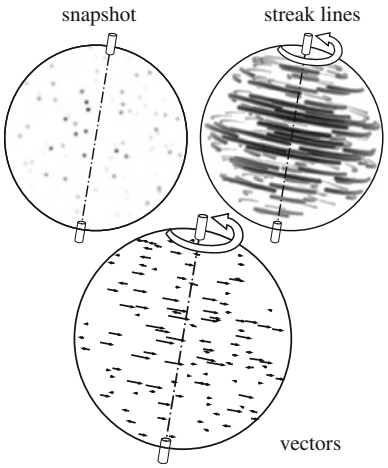

Fig. 6 Test sequence of a three-dimensional sphere rotating in space. The *grey values* are inverted to optimize the representation in this paper. On the *upper left*, the *dots in the sphere* are shown for a given position in time. Intensities of the particles are adjusted according to Eq. (2). On the *upper right*, streak lines of the particles for a rotating sphere are shown. The corresponding calculated vectors are shown below

To approximate the Poisson process of light collection on the chip, we simulated Gaussian independent, identically distributed noise of increasing variances between 1 and 6 levels of intensity for each experiment (Jähne 2002). The noise was added to the scene and values above and below the camera's intensity range were truncated. Finally, the intensities were quantized to 8 bit, i.e., to the values between 0 and 255.

As visualized in Fig. 6, the sphere was rotated with a constant angular speed of one degree in y-direction and 0.2 degrees in x-direction. The maximum speed of a particle was approximately 2.6 px per frame.

6 Error estimation

Due to the use of a classical PTV algorithm with sub-pixel accuracy for the wall-parallel velocity components, the corresponding error analysis can be referred to (Nobach 2004; Nobach and Honkanen 2005; Brady 2006). Errors specific to wall-PIV concern the distance between particles and the wall. Since the third velocity vector component v_z is derived from the particle depth D of two succeeding images $v_z = \frac{\Delta D}{\Delta t}$, the error in velocity can be directly attributed to the error in particle-wall distance.

For the error discussion, we have to keep in mind that a particle moves with its centre of mass at the corresponding particle depth D, whereas its position is measured by the distance to the wall of its surface R.

The final experimental result of our measurement is the particle depth D:

$$D = \frac{-1}{2\varepsilon c}\ln\left(\frac{I}{I_0}\right) + r_p \tag{5}$$

Therefore, according to Coleman Hugh and Steele (1989), the uncertainty U_D in the result is

$$U_D = \left[\left(\frac{\partial D}{\partial \varepsilon}U_\varepsilon\right)^2 + \left(\frac{\partial D}{\partial c}U_c\right)^2 + \left(\frac{\partial D}{\partial I}U_I\right)^2 + \left(\frac{\partial D}{\partial I_0}U_{I_0}\right)^2 + \left(\frac{\partial D}{\partial r_p}U_{r_p}\right)^2\right]^{\frac{1}{2}} \tag{6}$$

where the U_{Xi} are the uncertainties in the variables X_i, which are the uncertainties of the concentration c, of the extinction coefficient ε, of the intensity measurement I, of the incoming light intensity I_0, and of the particle radius r_p. As we are interested in the uncertainty of the wall-PIV measurement technique relative to its measurand D, we calculate the partial derivatives in eq. (6), divide by D and obtain:

$$\frac{U_D}{D} = \left[\left(\frac{r_p}{D} - 1\right)^2 \left(\left(\frac{U_\varepsilon}{\varepsilon}\right)^2 + \left(\frac{U_c}{c}\right)^2 \right) + \left(\frac{-1}{2\varepsilon c D}\right)^2 \left(\left(\frac{U_I}{I}\right)^2 + \left(\frac{U_{I_0}}{I_0}\right)^2 \right) + \left(\frac{1}{D} U_{r_p}\right)^2 \right)^{\frac{1}{2}} \quad (7)$$

Variations of the particles' radius and sphericity can cause errors in the calculated flow. Figure 7 illustrates the consequences of a negative deviation of the radius r_p of a single particle.

The uncertainty of the particle's radius is directly linked to the particle size distribution. This distribution was measured for a sample of 1320 particles. With the mean diameter of the sample population being 73.98 ± 0.19 µm, the precision limits of the particle radius r_p were measured at 3.43 µm. The precision limits of the mean particle diameter and the particle radius were calculated for a 95% confidence interval using two times the precision index of the sample population according to Mandel (1984).

For our light panel (see Sect. 3.2), fluctuations for I_0 of less than 1% were determined during tests over long periods of time (Schneider et al. 2008). The most important light instability is observed immediately after the illumination of the light panels due to temperature effects. A measurement of 3 min without prior warming up of the light panels and with maximal intensity settings would result in a relative uncertainty $\frac{U_{I_0}}{I_0}$ of 4.16%. After a warm up of 1 min, we already obtain a relative uncertainty of 1.07%. If the intensity decay is factored in (i.e., by using a reference target), the relative uncertainty caused by light fluctuations is smaller than 0.05%.

The intensity I is measured by a CCD or CMOS sensor. Its variation, due to sensor noise and discretization noise, has to be taken into account. According to Tropea et al. (2007), the noise to signal ratio, depending on the sensor type, is between 1 and 10%. Measurements by our high-speed camera against a constant light source resulted in a relative uncertainty of 2.6%.

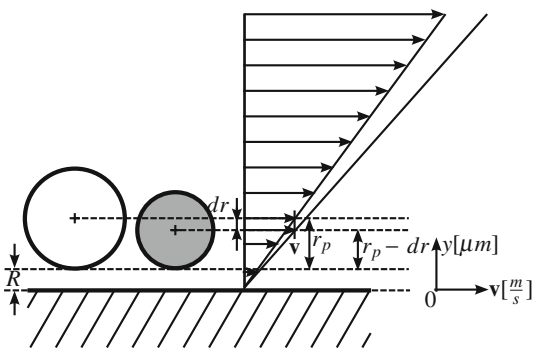

Fig. 7 Influence of an assumed radius of a single particle (*grey, right*) which differs from the real radius of the single particle (*white, left*) on the shear stress. The velocity corresponding to the distance to the wall $D = R + r_p$, $\mathbf{v}(D)$, is allotted to the distance to the wall $R + r_p - dr$

The extinction $E = \varepsilon \cdot c \cdot R$ of a fluid has an impact on U_D through the dye concentration c and the extinction coefficient ε.

As mentioned before, use of a molecular dye inhibits the local aberrations of a given dye concentration. However, the concentration of the absorbing molecules in a molecular dye may vary for different trading units (according to EC directive 2008/128/EG, the percentage of dye in food colours may vary, see e.g. (DFG Farbstoffkommission 1988)). Therefore, the extinction spectrum of the dye has to be assured by a photometric investigation. Our dye was tested with the two beam photometer Specord 205, Analytik Jena AG, Jena, Germany (see Fig. 2). Furthermore, the dye concentration in the test fluid can vary according to the accuracy of the fluid preparation. Let us assume the preparation of 1 l of test fluid with 0.3 g dye. To simplify matters, the preparation will be done without dilution series. Using a volumetric flask of 1,000 ± 0.4 ml and an analytical balance that measures masses to within 0.001 g, we obtain a relative uncertainty of 0.34%.

The extinction can also be falsified by the assumption of a faulty extinction coefficient ε. Since we measured the wavelength-dependent spectrum of our dye, we know the wavelength-dependent extinction coefficient with the exactitude of the photometric reference measurement. The preparation used a 1:100 dilution series and had a relative uncertainty of less than 0.1%. However, as the used dye has a spectral selectivity, the value of ε is a function of the wavelength of the absorbed light. By using a light panel of LEDs, the absorbed light is not exactly monochromatic but has a spectrum. The given wavelengths of our red (627 nm) and red-orange (617 nm) LEDs are only the corresponding dominant wavelengths.

Modifications of the LED spectrum, such as a shift of several nanometres, result in a modified assignment between the LED spectrum and the spectrum of the dye. This may be caused either by a selective absorption of the flow model or by different electrical currents, temperature effects and spectral degradation over time (Buermen et al. 2008). The resulting error depends heavily on the gradient of the extinction coefficient in the region of the spectrum. The lower the gradient of ε, the lower the error becomes for a modified spectrum. For the dye patent blue V, the two used spectra red and red-orange are located at a maximum, covering the major part of the two spectra. For an estimation of the related uncertainty, we assign the shift between the two spectra to the uncertainty of the extinction coefficient. In order to discuss the derivation of this uncertainty, we have to introduce the spectra into Eq. (2).

For each wavelength of the spectrum, Eq. (2) is valid. However, we can only measure the total intensity of the

reflected light. Therefore, the wavelength of a light spectrum λ_i with $i = 1n$, the corresponding emitted intensities $I_{0,i}$, the wavelength-dependent extinction coefficients ε_i and the resulting emitted light intensities I_i can be introduced in Eq. (2). For numerical calculations, we discretized the spectrum into a set of wavelengths with a width of 1 µm each (see below). Knowing that the sum of the emitted light intensities equals the total emitted light intensity, we obtain:

$$I = \sum_{i=1}^{n}(I_i) = \sum_{i=1}^{n}(I_{0,i} \cdot e^{-2\cdot\varepsilon_i\cdot c\cdot R}) \tag{8}$$

By normalizing the intensities $I_{0,i}$ of our emitted light spectrum to 1 with the relative intensities $\imath_{0,i}$ with $I_0 = \sum_{i=1}^{n}(I_{0,i}) = I_0 \cdot \sum_{i=1}^{n}(\imath_{0,i})$, Eq. (8) can be rewritten to:

$$I = I_0 \cdot \sum_{i=1}^{n}(\imath_{0,i} \cdot e^{-2\cdot\varepsilon_i\cdot c\cdot R}) \tag{9}$$

Using this equation, we can calculate the particle-wall distance R if I_0 is known by calibration. In order to obtain a good numerical approximation of the analytical solution of Eq. (9), we use a lookup table with results of the sum term $\sum_{i=1}^{n}(\imath_{0,i} \cdot e^{-2\cdot\varepsilon_i\cdot c\cdot R})$ for the values R in the depth of view with an increment of 1 µm. The conversion of the light intensity to the corresponding pixel grey value ϕ at the coordinates $[m, n]$ is given by Eq. (10) according to Westerweel (2000):

$$\phi[m,n] = \gamma \cdot d_r^2 \cdot I(X_m, Y_m) + v_{m,n} \tag{10}$$

In this equation, the parameter γ converts between an image exposure and the resulting grey value. I stands for the exposure per unit area on the image sensor. A sensor's position is given by X_m and Y_m, calculated by given coordinates $[m, n]$ times the pixel dimension d_r. Sensor noise and discretization noise are represented by v and will be set to zero for the calculation of R. Searching an R for a given ϕ means looking up the minimum of $\phi_0 \cdot \sum_{i=1}^{n}(\imath_{0,i} \cdot e^{-2\cdot\varepsilon_i\cdot c\cdot R}) - \phi$, for which the sum term has already been calculated. Consequently, we have a fast algorithm from the result of which we can directly define the maximal error in depth resulting from the increment in the lookup table.

For an uncertainty estimation of the extinction coefficient, we shifted our spectrum by 2 nm. This shift corresponded to maximal shifts during spectral measurements in dependence of light intensity and the amperage of our light panels. Using Eq. (9) on the calibration data of Sect. 4.1, we compared the results with a shifted spectrum to the results without a shifted spectrum. We obtained a relative uncertainty of 0.12%.

At this point, the relative uncertainty of the measurement relative to the measureand R can be calculated by Eq. (7). For a particle almost touching the wall, we obtain a relative uncertainty of 10%. This uncertainty drops down to 5% for a distance of 38 µm between wall and particle surface and reaches 2% for a distance of 150 µm between wall and particle surface. The relative uncertainty of the measurement is dominated by the uncertainty of the particle radius. This uncertainty is five times higher than the next important uncertainty of the intensity I, caused by the CCD camera. The influence of all other uncertainties stays below 0.5%.

The knowledge of I_0 may pose a problem for non-planar inner surfaces. One source of errors could be different refractive indices resulting in different partial reflections on the vaulted surfaces. These errors are inhibited by matching the refractive indices of flow model and fluid. Further errors could result from different material thicknesses. The outer surfaces of our models are kept planar so that the interface between model and air is plane. In case of different material thicknesses, light absorption by the wall can lead to different, unknown light intensities I_0. For the silicone material used for the fabrication of our flow models, the fraction of the absorbance α, with $\alpha = \frac{E}{c}$ relative to the absorbance of the used fluid, is smaller than 0.16%. This means, that a difference in wall thickness of 2 cm corresponds to a maximal error of one grey value at an intensity corresponding to 255 grey values. If necessary, one possibility to overcome the resulting errors for a spectral non-selective material would be the use of the two wavelength (bichromatic) method presented in (Jehle and Jähne 2008). Illuminating a particle at a given depth R, with two different wavelengths A and B, with two different spectra S_A and S_B and with diverging corresponding extinctions, we can modify Eq. (9) so that it no longer depends on the emitted intensities $I(A)_0$ and $I(B)_0$ but on their fraction:

$$\frac{I(A)}{I(B)} = \frac{I(A)_0}{I(B)_0} \cdot \frac{\sum_{i=1}^{n}(\imath(A)_{0,i} \cdot e^{-2\cdot\varepsilon_i\cdot c\cdot R})}{\sum_{i=1}^{n}(\imath(B)_{0,i} \cdot e^{-2\cdot\varepsilon_i\cdot c\cdot R})} \tag{11}$$

Since the fraction $\frac{I(A)_0}{I(B)_0}$ does not change by an extinction of a spectral non-selective material (i.e., the silicone of our flow models), R does not depend on the material thickness. It has to be noted that the bichromatic wall-PIV approach is not as equally fail-safe as the monochromatic approach relating to the extinction coefficient. The reason is that the quotient of exponentials in Eq. 11 depends on the difference between the two spectra. Similar spectral absorbances lead to small values for the quotient and to a strong dependence on the spectral accuracy. If the bichromatic approach has to be used, it is advisable to calibrate the measurement system for each measurement series or to use another combination of dye and spectra, for example that of (Jehle and Jähne 2008).

7 Results and discussion

7.1 Calibration

The calculated positions, using the exact parameters and errors for a wrong dye concentration and wrong light intensities, previously discussed in Sect. 6, are shown in Fig. 8.

The total mean error of the measured particle-wall distances from the real particle-wall distances was 1.67 µm. For the SPS, 1.67 µm is below the exactitude of the used measurement dial (and thereby the particle positioning) and proves the ability to reconstruct the particle depth. Assuming an erroneous concentration or a wrong reference grey value ϕ_0 leads to the presented gradient or offset errors, which are shown in Fig. 8. Therefore, a calibration with a single particle assures a minimization of bias.

7.2 Inclined single particle traversal

For the inclined single particle traversal, the horizontal and vertical positions of the particle were estimated with a PTV algorithm with sub-pixel interpolation as well as with the trajectory approach that uses the PTV calculation as an initial guess. Both results are shown in Fig. 9, where the PTV results are given by the triangles and the trajectory calculations are represented by the crosses. The target value is given by the solid line. In the graph of Fig. 9, we can see that the results of PTV and trajectory flow estimation have a similar quality up to a particle depth of 128 µm (distance between the particle surface and the wall). For particle positions with a higher particle-wall distance, the PTV calculation does not match the particle any longer. For the trajectory flow estimation, we obtained good estimates for the particle positions up to a depth of 150 µm. The absolute mean error of the horizontal position estimation was 2.75 µm (0.0495 px) for PTV and 1.42 µm (0.0255 px) for the trajectory calculations. We can see that the trajectory calculations lead to a significant improvement of the horizontal flow estimation. The absolute mean error of the vertical position was 7.52 µm (0.077 logarithmic grey values) for PTV and slightly better with 7.16 µm (0.074 logarithmic grey values) for the trajectory calculations or about 10% of the particle's diameter. The error for the vertical (depth) movement is approximately five times higher than the error for the horizontal (wall parallel) movement. Furthermore, the results of both graphs show the dependence of the flow estimation on the particle grey value. With a higher particle to wall distance, the signal to noise ratio becomes a challenge for the flow estimation algorithms.

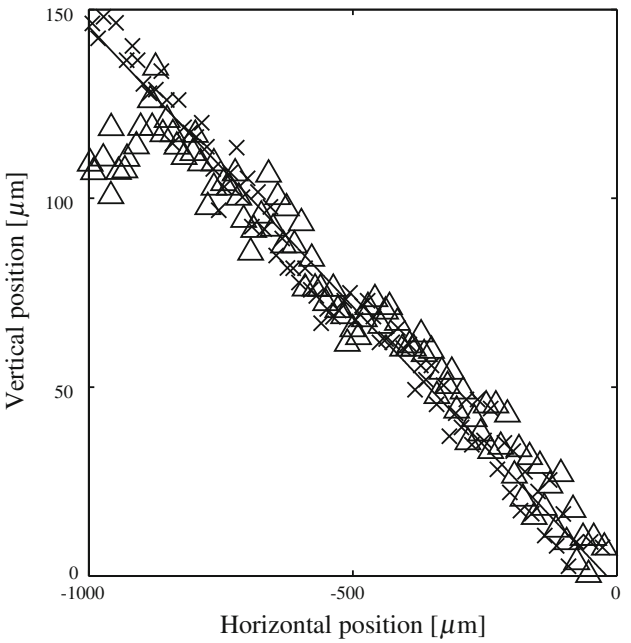

Fig. 9 Estimated horizontal and vertical flow positions. Estimations by the PTV algorithm are marked with *triangles*, estimations using the trajectories are marked with *crosses*. The *solid line* represents the adjusted particle movement

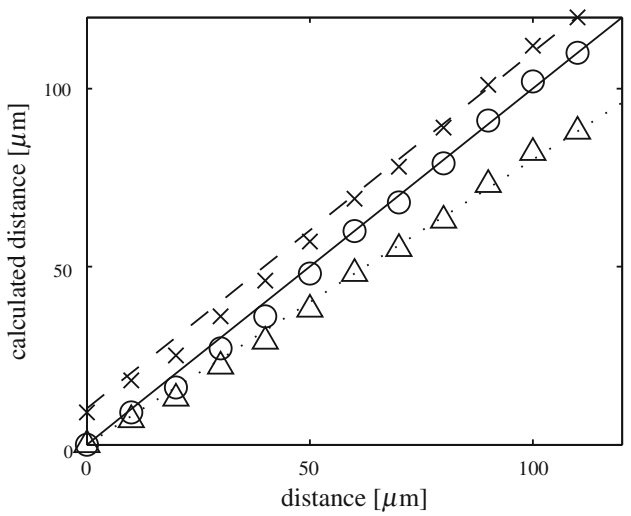

Fig. 8 Distances, calculated with Eq. (9) from the measured *grey values* of one particle, are presented by *circles*. The total mean error of the theoretical result, given by the *solid line*, is 1.67 µm. Underestimating the concentration of patent blue V by 20% would lead to the *triangles* and the corresponding *dotted line*. For an overestimation of 20 *grey values* for the grey value ϕ_0 of the emitted intensity I_0, we would obtain an error of 6.67 µm, given by the *crosses* and the corresponding *dashed line*

7.3 Artificial data sets

The results for each noise level are shown in Fig. 10. The error measure used is the so-called endpoint error (Baker et al. 2007), which is the length of the difference vector

between the estimated and the true 2D-flow vector. Since the initial guess is a standard PTV algorithm, we use it as reference data for comparison. To capture all the details of the error statistics, we did not compute the mean and standard deviation. Instead, we computed the results for one frame of our test sequences and sorted all occurring errors to visualize the full statistical information. As can be seen in Fig. 10 for a noise level of one intensity, the initial guess cannot be improved very much by our algorithm, as it is already very good. For errors below 0.05 px our algorithm performs slightly worse, whereas for values above it performs slightly better. Similar results can be observed at higher noise levels, only that the improvement for errors larger than 0.05 px becomes much more obvious: For example, with a noise level of 4 intensities our algorithm yields 80% of particles with errors below 0.15 px while the initial guess has only 50% of particles below this threshold.

Unfortunately, when the initial guess is bad (an error of more than 0.5 px), our algorithm increases the error in approximately 1 to 5% of cases. This happens, for example, when particles overlap each other. However, such situations could be detected by comparing the initial guess with the result optimized by rejecting all other optimizations, where the difference between both is larger than e.g. 0.5 px.

7.4 Error estimation

In chapter 6, the error of wall-PIV concerning the distance between particles and the wall was estimated. Here, we discuss the impact of hydrodynamic forces influencing the wall-PIV error estimation specifically concerning the ability of particles to follow the flow in the case of particle-wall interaction. This ability has been vastly investigated for classical PIV (see e.g. (Westerweel 1993; Melling 1997; Raffel et al. 1998)). These investigations for classical PIV use mainly the Basset-Boussinesq-Oseen equation, assuming unbounded liquid flow conditions. The equation does not consider particle-wall interaction. The particle-wall interaction may affect the particles' ability to follow the flow and has to be taken into account for the wall-PIV measurement technique. This means that additional hydrodynamic forces, such as the Magnus force due to particle rotation and the Saffman force caused by shearing, should be considered. Both lift forces cause a transversal movement of the particles. Many investigations concerning this topic have been done (see e.g. Michaelides 2003; Loth 2000). The particles' movement incorporating lift forces can be estimated with the help of equations proposed by either Cherukat and McLaughlin (1994) or Magnaudet (2003). These equations, however, require knowledge of

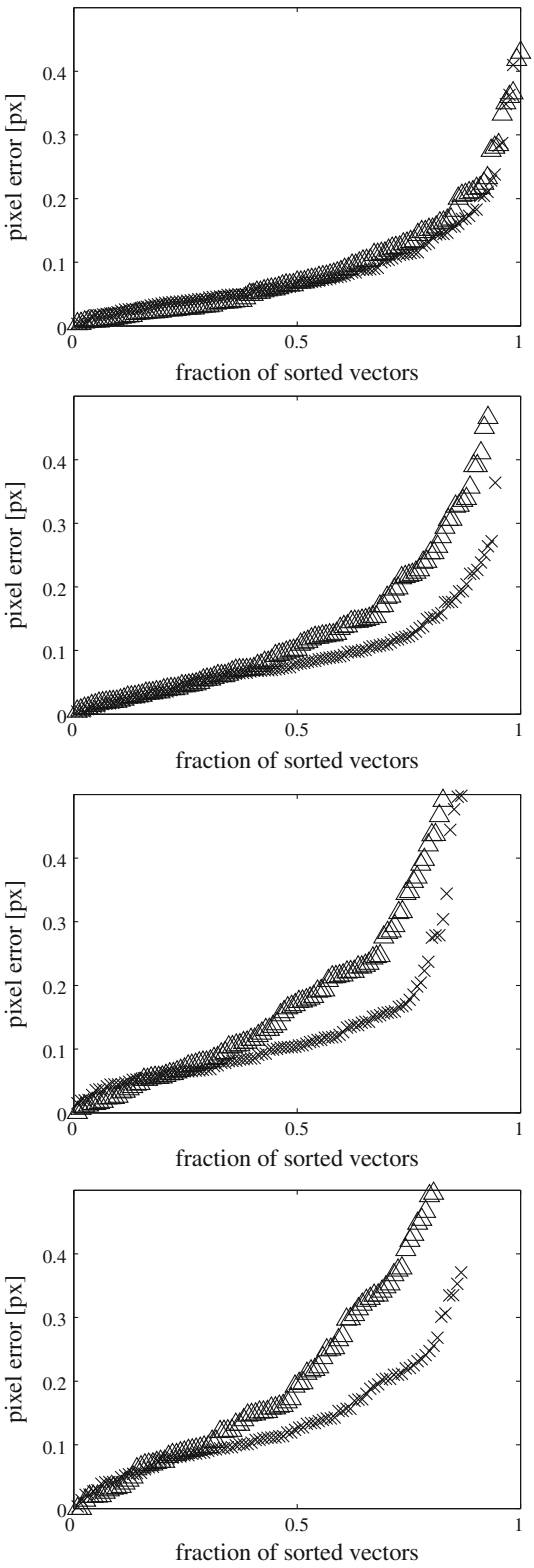

Fig. 10 Sub-pixel errors for noise levels of 1 (on *top*), 2, 4, and 6 *grey values* sorted according to magnitude. Results of the PTV algorithm are marked with *triangles*, those of the trajectory calculations by *crosses*

the fluid velocities and the particle wall distances. The impact of lift forces was also experimentally investigated for tube flow: No measurable migration of particles (polystyrene spheres with a radius of 100 μm) for traveled distances between 350 and 3,500 cm at a particle Reynolds number of $Re_p \leq 10^{-6}$ was found (Goldsmith and Mason 1962; Karnis et al. 1963). The particle Reynolds number was calculated with the particles' diameter and slip velocity at the tube centre. They concluded that rigid and spherical particles lead to noticeably smaller lift forces (Goldsmith and Mason 1962; Karnis et al. 1963). In contrast, significant radial migration was found in the case of deformable particles (e.g. Goldsmith and Mason 1962; Karnis et al. 1963) and in the case of rigid particles with $Re_p \geq 10^{-3}$ (e.g. (Segre and Silberberg 1962a, b). Furthermore, the particle-wall interaction results in an increased drag force that can be incorporated by a correction parameter as a function of the particle diameter to particle-wall distance relationship (e.g. Young and Hanratty 1991). This correction parameter adapts the classical PIV consideration of the error estimation for the wall-PIV technique. Increased drag force increases relaxation time, a parameter used to estimate the ability of a particle to follow the flow. Note that both effects (lift and drag forces) can be reduced by matching the particle/fluid density relation.

8 Conclusions

The wall-PIV technique allowing time-resolved 3D-3C measurement of the flow fields near vaulted and/or deformable walls was presented and its exactitude evaluated by error propagation. Quantitative results of depth error estimations for the relevant input parameters, such as light intensities or sensor noise (for our setup about 3 μm each), were presented. Furthermore, the new flow estimation algorithm based on learned particle trajectories allowing 3D-3C flow estimation was introduced. Note, earlier algorithms were 3D-2C techniques.

First, the wall-PIV technique was calibrated with a single particle setup for the grey value based assessment of the particle-wall distance. This experiment allows us to investigate the difference between set points of the distance between a tracer and the wall and the corresponding measured distances. The resulting mean error was very low with 1.67 μm or 2.29% of the particle's diameter. The accuracy of the flow estimation algorithm was initially tested with a single particle setup in the inclined particle traversal experiment and then tested with the artificial data set simulating a rotating sphere. The achieved accuracy of the horizontal movement was comparable with the accuracy of the PTV and PIV measurement techniques (0.0255 px). The achieved accuracy of the vertical position assessment was 5 times lower. Comparing these results with an error obtained during the calibration procedure, we can conclude that the wall-PIV setup and the flow estimation algorithm have potential and should be further optimized. An analytical error estimation showed relative measurement uncertainties of 2 to 10% in dependence of the distances between particles and wall. The magnitude of the relative uncertainty is inversely proportional to the particles' distances to the wall. This is mainly caused by the uncertainty in particle radius and, with five times lower impact, by the uncertainty caused by the recording camera. Therefore, the exactitude of the measurements will be increased in the future by a higher degree of monodispersity of the particles and a higher signal to noise ratio of the camera.

The next step in the development of the wall-PIV technique is the validation with a known 3D flow case. The existing exact solutions of the Navier Stokes equations provide either only two components of a flow or are not applicable to reference experiments (Hui 1987; Ethier and Steinman 1994). Lacking a 3D-3C experiment with a known analytical solution, a rotating flow generated by confined rotating disks with an analytical solution for the tangential velocity components according to Khalili and Rath (1994), has been chosen. This flow case was also selected because it is similar to that of displacement blood pumps during their late suction phase. These experimental studies, which also should be supported by measurements using a classical PIV technique with a laser sheet parallel to the rotating disk, are now under preparation.

Acknowledgments We gratefully acknowledge the support of the Deutsche Forschungsgemeinschaft DFG within the research program SPP 1147. We also thank the MFG, TU Berlin for their support.

References

Adrian RJ, Yao CS (1985) Pulsed laser technique application to liquid and gaseous flows and the scattering power of seed materials. In: Proceedings of the international symposium on applications of laser anemometry to fluid mechanics, vol. 24, pp. 44–52

Affeld K, Goubergrits L, Kertzscher U, Gadischke J, Reininger A (2004) Mathematical model of platelet deposition under flow conditions. Int J Artif Organs 27(8):699–708

Atkinson CH, Dillon-Gibbons CJ, Herpin S, Soria J (2008) Reconstruction techniques for tomographic piv (tomo-piv) of a turbulent boundary layer. In: Proceedings of the 14th international symposium on applications of laser techniques to fluid mechanics. Lisbon, Portugal

Baker S, Roth S, Scharstein D, Black M, Lewis J, Szeliski R (2007) A database and evaluation methodology for optical flow. In: Proceedings of the international conference on computer vision, pp. 1–8

Berthe A, Kondermann D, Christensen C, Goubergrits L, Kertzscher U (2007) Using single particles for the validation of a 3d-3c near wall measurement technique. In: The 7th international symposium particle image velocimetry. Rome, Italy

Berthe A, Weber S, Kondermann D, Goubergrits L, Kertzscher U (2008) Application of the wall-piv technique on cerebral aneurysm models. In: The 13th international symposium on flow visualization. Nice, France

Brady MR (2006) Subpixel resolution schemes for multiphase flows. Master's thesis, Virginia Polytechnic Institute and State University

Bruecker C (1995) Digital-particle-image-velocimetry (dpiv) in a scanning light-sheet: 3d starting flow around a short cylinder. Exp Fluids 19(4):255–263

Buermen M, Pernus F, Likar B (2008) Led light sources: a survey of quality-affecting factors and methods for their assessment. Meas Sci Technol 19(12):122,002–122,017

Cherukat P, Mclaughlin JB (1994) The inertial lift on a rigid sphere in a linear shear flow field near a flat wall. J Fluid Mech Digit Arch 263(1):1–18

Coleman Hugh W, Steele WG (1989) Experimentation and uncertainty analysis for engineers. Wiley-Interscience, New York, pp 42

Cowen EA, Monismith SG, Cowen EA, Monismith SG (1997) A hybrid digital particle tracking velocimetry technique. Exp Fluids 22(3):199–211

Debaene P, Kertzscher U, Goubergrits L, Affelt K (2005) Visualization of a wall shear flow: Development of a new particle image interrogation method. J VISUAL-JAPAN 8:285–364

DFG Farbstoffkommission (1988) Farbstoffe fuer lebensmittel, 2nd edn. VCH Verlagsgesellschaft, Weinheim, Germany

Elsinga G, Scarano F, Wieneke B, van Oudheusden B (2006) Tomographic particle image velocimetry. Exp Fluids 41(6): 933–947

Ethier CR, Steinman DA (1994) Exact fully 3d navier-stokes solutions for benchmarking. Int J Numer Methods Fluids 19(5):369–375

Fomin NA (1998) Speckle Photography for Fluid Mechanics Measurements. Springer, Heidelberg

Goldsmith HL, Mason SG (1962) The flow of suspensions through tubes. i. single spheres, rods, and discs. J Colloid Sci 17(5): 448–476

Goubergrits L, Affeld K, Fernandez-Britto J, Falcon L (2002) Atherosclerosis and flow in carotid arteries with authentic geometries. Biorheology 39(3-4):519–524

Goubergrits L, Weber S, Petz C, Spuler A, Pöthke J, Berthe A, Hege H-C (2009) Wall-piv as a near wall flow validation tool for cfd. J Visual 12(3):241–250

Graff EC, Pereira F, Gharib M (2008) Defocusing digital particle image velocimetry: a volumetric dpiv technique for dual and single phase flows. In: Proceedings of the 14th international symposium on applications of laser techniques to fluid mechanics. Lisbon, Portugal

Hill D, Troolin D, Walters G, Lai W, Sharp K (2008) Volumetric 3-component velocimetry (v3v) measurements of the turbulent flow in stirred tank reactors. In: Proceedings of the 14th international symposium on applications of laser techniques to fluid mechanics. Lisbon, Portugal

Hinsch KD (2002) Holographic particle image velocimetry. Meas Sci Technol 13(7):R61–R72

Horn B, Schunck B (1981) Determining optical flow. Artif Intel 17: 185–204

Hui WH (1987) Exact solutions of the unsteady two-dimensional navier-stokes equations. Zeitschrift für Angewandte Mathematik und Physik (ZAMP) 38(5):689–702

Jähne B (2002) Digital image processing, 5th edn. Springer Verlag, Berlin, pp 91–94

Jehle M, Jähne B (2008) A novel method for three-dimensional three-component analysis of flows close to free water surfaces. Exp Fluids 44(3):469–480

Jehle M, Jähne B, Kertzscher U (2006) Direct estimation of the wall shear rate using parametric motion models in 3d. Pattern recognition pp. 434–443

Kaehler CJ, Kompenhans J (2000) Fundamentals of multiple plane stereo particle image velocimetry. Exp Fluids 29(7):S070–S077

Karnis A, Goldsmith HL, Mason SG (1963) Axial migration of particles in poiseuille flow. Nature 200(4902):159–160

Keane RD, Adrian RJ (1990) Optimization of particle image velocimeters. i. double pulsed systems. Meas Sci Technol 1(11):1202–1215

Keane RD, Adrian RJ, Zhang Y (1995) Super-resolution particle imaging velocimetry. Meas Sci Technol 6(6):754–768

Kertzscher U, Affeld K, Goubergrits L, Schade M (1999) A new method to measure the wall-shear rate in models of blood vessels. In: Proceedings of the European medical and biological engineering conference 1999, 2, pp. 1412–1413

Kertzscher U, Berthe A, Goubergrits L, Affeld K (2008) Particle image velocimetry of a flow at a vaulted wall. Proceedings of the Institution of Mechanical Engineers, Part H: J Eng Med 222(4): 465–473

Khalili A, Rath HJ (1994) Analytical solution for a steady flow of enclosed rotating disks. Zeitschrift fr Angewandte Mathematik und Physik (ZAMP) 45(4):670–680

Kim MC, Nam J, Lee CS (2006) Near-wall deposition probability of blood elements as a new hemodynamic wall parameter. Annal Biomed Eng 34(6):958–970

Kim S, Lee S (2008) Effect of particle number density in in-line digital holographic particle velocimetry. Exp Fluids 44(4): 623–631

Köhler U, Marshall I, Robertson MB, Long Q, Xu XY, Hoskins PR (2001) Mri measurement of wall shear stress vectors in bifurcation models and comparison with cfd predictions. J Magn Reson Imag 14(5):563–573

Kondermann D, Kondermann C, Berthe A, Kertzscher U, Garbe C (2008) Motion estimation based on a temporal model of fluid flows. In: Proceedings of the 13th international symposium on flow visualization. Nice, France

Lai W, Pan G, Menon R, Troolin D, Graff E, Gharib M, Pereira F (2008) Volumetric three-component velocimetry: a new tool for 3d flow measurement. In: Proceedings of the 14th international symposium on applications of laser techniques to fluid mechanics. Lisbon, Portugal

Loth E (2000) Numerical approaches for motion of dispersed particles, droplets and bubbles. Prog Energ Combust Sci 26(3):161–223

Maas HG, Gruen A, Papantoniou D (1993) Particle tracking velocimetry in three-dimensional flows. Exp Fluids 15(2): 133–146

Magnaudet J (2003) Small inertial effects on a spherical bubble, drop or particle moving near a wall in a time-dependent linear flow. J Fluid Mech 485:115–142

Malik NA, Dracos T, Papantoniou DA (1993) Particle tracking velocimetry in three-dimensional flows. Exp Fluids 15(4): 279–294

Mandel J (1984) The statistical analysis of experimental data. Dover Pubn Inc, Mineola, NY

Marxen M, Sullivan PE, Loewen MR, Jähne B (2000) Comparison of gaussian particle center estimators and the achievable measurement density for particle tracking velocimetry. Exp Fluids 29(2):145–153

Melling A (1997) Tracer particles and seeding for particle image velocimetry. Meas Sci Tech 8(12):1406

Michaelides EE (2003) Hydrodynamic force and heat/mass transfer from particles, bubbles, and drops—the freeman scholar lecture. J Fluids Eng 125(2):209–238

Michaelis D, Wieneke B (2008) Comparison between tomographic piv and stereo piv. In: Proceedings of the 14th international symposium on applications of laser techniques to fluid mechanics. Lisbon, Portugal

Modarress D, Svitek P, Wilson D (2005) Micro-optical sensor use in boundary layer flows with polymers and bubbles. In: Proceedings of the 2nd international symposium on seawater drag reduction

Nobach H (2004) Accuracy of sub-pixel interpolation in piv and ptv image processing. Technical University of Darmstadt, Darmstadt, Germany, pp 114–130

Nobach H, Honkanen M (2005) Two-dimensional gaussian regression for sub-pixel displacement estimation in particle image velocimetry or particle position estimation in particle tracking velocimetry. Exp Fluids 38(4):511–515

Park H, Moore JA, Trass O, Ojha M (1999) Laser photochromic velocimetry estimation of the vorticity and pressure field–two-dimensional flow in a curved vessel. Exp Fluids 26(1):55–62

Raffel M, Willert C, Kompenhans J (1998) Particle image velocimetry. A practical guide. Springer, Heidelberg

Ruck B (2003) Color-coded tomography. In: 7th Int. symp. on fluid control, measurement and visualization

Ruhnau P, Schnörr C (2007) Optical stokes flow estimation: an imaging-based control approach. Exp Fluids 42(1):61–78

Schneider T, Goubergrits L, Kertzscher U, Paschereit Christian O (2008) Development of a new 3d shear stress measurement technique using the birefringence. In: Proceedings of the 14th international symposium on applications of laser techniques to fluid mechanics

Schroeder A, Geisler R, Elsinga G, Scarano F, Dierksheide U (2008) Investigation of a turbulent spot and a tripped turbulent boundary layer flow using time-resolved tomographic piv. Exp Fluids 44(2):305–316

Segre G, Silberberg A (1962a) Behaviour of macroscopic rigid spheres in poiseuille flow part 1. determination of local concentration by statistical analysis of particle passages through crossed light beams. J Fluid Mech Digit Arch 14(01), 115–135 M3. doi:10.1017/S002211206200,110X

Segre G, Silberberg A (1962b) Behaviour of macroscopic rigid spheres in poiseuille flow part 2. experimental results and interpretation. J Fluid Mech Digit Arch 14(01):136–157 M3. doi:10.1017/S0022112062001,111

Sheplak M, Cattafesta L, Nishida T (2004) Mems shear stress sensors: promise and progress. In: 24th AIAAA aerodynamic measurement technology testing conference. Florida Univ Gainesville mechanical and aerospace engineering

Takeda Y (1999) Ultrasonic doppler method for velocity profile measurement in fluid dynamics and fluid engineering. Exp Fluids 26(3):177–178

Triep M, Brücker C, Schröder W (2005) High-speed piv measurements of the flow downstream of a dynamic mechanical model of the human vocal folds. Exp Fluids 39(2):232–245

Tropea C, Yarin AL, Foss JF (ed) (2007) Springer Handbook of Experimental Fluid Mechanics. Springer-Verlag, Berlin, Heidelberg, Germany

Westerweel J (1993) Digital particle image velocimetry. Ph.D. thesis, Technical University of Delft

Westerweel J (2000) Theoretical analysis of the measurement precision in particle image velocimetry. Exp Fluids 29(7): S003–S012

Xie MX, Wang XF, Cheng TO, Lu Q, Yuan L, Liu X (2005) Real-time 3-dimensional echocardiography: A review of the development of the technology and its clinical application. Prog Cardiovas Dis 48(3):209–225

Young JB, Hanratty TJ (1991) Trapping of solid particles at a wall in a turbulent flow. AIChE J 37(10):1529–1536